Effects of Water and Gas Compositions on the Internal Corrosion of Gas Pipelines—Modeling and Experimental Studies

N. Sridhar, D.S. Dunn, A.M. Anderko, M.M. Lencka,** and H.U. Schutt****

ABSTRACT

Results of a laboratory study of internal corrosion in wet gas pipelines under conditions involving a stagnant or slowly flowing aqueous phase indicate that the corrosion rate is not affected by calcium and magnesium scale-forming tendency of the test solutions, provided that they are buffered. It is possible that the scales formed are sufficiently porous to permit electrolyte contact with steel. However, an increase in pH and decrease in oxygen resulted in significant corrosion rate reduction. Thermodynamic analyses indicate that the formation of metastable iron sulfide (FeS) precipitates is promoted by higher pH and higher dissolved iron concentration, and hindered by the presence of carbon dioxide (CO_2). The presence of oxygen on corrosion may lead to the transformation of a metastable FeS phase, mackinawite ($Fe_{1+x}S$), to another metastable phase, greigite (Fe_3S_4). Electrochemical polarization data indicate that the steel behaves in an active manner symptomatic of a nonprotective corrosion product film. The effect of oxygen in increasing the corrosion rate may be related to the increase in corrosion potential. Surface analysis by Raman spectroscopy confirmed some of the thermodynamic predictions of stable phases. Additionally, Raman spectroscopy indicated the predominance of akaganeite (β-) and repidocrocite (γ-FeOOH). Based on the results of this study, a regression equation developed from nonscale-forming solutions may be adopted for predicting the internal corrosion of gas transmission and gathering lines caused by condensed water and acid gases.

KEY WORDS: carbon dioxide, hydrogen sulfide, natural gas, oxygen, Raman spectroscopy, scaling, thermodynamic modeling

INTRODUCTION

The ability to safely transport wet, untreated natural gases through pipelines offshore or at other inaccessible locations is an important factor in the development of new gas fields. The internal corrosion rate of steel pipelines varies in a complex way with the gas composition—specifically carbon dioxide (CO_2), O_2, and hydrogen sulfide (H_2S) partial pressures—and condensed water chemistry. Estimating the corrosion rate of steel at inaccessible locations from the analysis of the gas and water composition will enable a better determination of the need for corrosion inhibitors. Quantitative understanding of the corrosion rate of steel under these conditions will be key to an accurate risk assessment of pipelines from internal corrosion.

Corrosion in gas gathering and transmission lines has been reported in the presence of H_2S and CO_2 in the gas and high chloride concentrations or sulfur/polysulfide sludge from the formation water.[1-2] While O_2-induced corrosion of gas transmission or gathering lines has not been reported, a wide range of O_2 concentration limits can be found in the gas industry. A 1988 survey of 44 natural gas transmission pipeline companies indicated that the gas quality specifications allowed maximum O_2 concentrations ranging from < 10 vol% to 1.0 vol%.[3] The actual concentrations of O_2 in the gas stream were

Submitted for publication April 2000; in revised form, November 2000.

* CNWRA, Southwest Research Institute, San Antonio, TX.
** OLI Systems, Inc., Morris Plains, NJ.
*** Consultant, Houston, TX.

0010-9312/01/000045/$5.00+$0.50/0

TABLE 1
The Types of Iron Sulfides Generally Observed and their Crystal Structures

Sulfide	Chemical Formula	Stoichiometry	Crystal Structure
Mackinawite	$Fe_{1+x}S$	x = 0.057-0.064	Tetragonal
Pyrrhotite	$Fe_{1-x}S$	x = 0 to 0.14	Variable
Greigite	Fe_3S_4	—	Cubic
Smythite	$Fe_{3+x}S_4$	x = 0 to 0.25	Hexagonal
Pyrite	FeS_2	S or Fe deficient	Cubic
Marcasite	FeS_2	S deficient, unstable	Orthorhombic

low, 0 vol% to 0.02 vol%. However, the typical O_2 concentrations in the natural gas pipelines are believed to be rising, particularly in lines transporting gases pumped from storage fields and from fields being produced under vacuum. At present, little is known of the safe and economical limits of O_2. The objectives of the research presented in this paper are to understand the effects of water chemistry and gas composition on corrosion through thermodynamic and kinetic analyses and to determine the effect of scale-forming species in the water on corrosion. These effects are examined through a combination of experimental investigation and thermodynamic modeling.

LITERATURE REVIEW

CO_2 Corrosion — Dissolved CO_2 forms carbonic acid (H_2CO_3), which then increases the cathodic reaction kinetics by dissociation to bicarbonate. Under stagnant conditions, dissolved ferrous ions combine with the H_2CO_3 to form ferrous carbonate (siderite; $FeCO_3$). However, under flow conditions, parts of the $FeCO_3$ scale may be removed, resulting in an increased corrosion rate of the steel attributable to the H_2CO_3. DeWaard and Milliams developed a semi-empirical correlation between corrosion rate under flowing conditions (≈ 1 m/s at the metal surface) and CO_2 partial pressure.[4] This relationship was later simplified in the form of a nomogram by DeWaard, et al.:[5]

$$\log(\text{c.r.,mm / y}) = 5.8 - \frac{1780}{T} + 0.67\log(pCO_2) \qquad (1)$$

Equation (1) provides a conservative estimate of corrosion rate under flowing conditions because it does not account for the effect of nonideality of the gas phase and scale formation. The effect of total pressure of gas and $FeCO_3$ scale formation on decreasing the corrosion rate was given in terms of correction factors.[5] One of the major limitations of this approach is that the correction factors attributable to scale formation, pH, and total iron concentration are not considered in terms of a consistent thermodynamic speciation model. Other correlations have been presented in a recent review of the literature that apply to flowing solutions containing a CO_2/H_2S ratio > 200 although no rationale is provided for this cutoff in the ratio.[6] Pitting was observed when the pH was allowed to attain its natural value (~ 4) whereas no pitting was seen when the pH was controlled at a value of ~ 6 using bicarbonate.[6]

H_2S Corrosion and Iron Sulfides — A small concentration of H_2S in the gas stream is generally believed to be beneficial because of the formation of a protective iron sulfide film. Shoesmith, et al., examined the behavior of iron and steel in aqueous sulfide solutions because of its importance to the Girdler-Sulfide process used to produce heavy water in the Canadian nuclear program.[7-8] In strongly alkaline conditions, steel was passivated by an oxide film that might have contained deposited sulfur in the pores, but no sulfide was detected.[7] In solutions of pH ranging from 9 to 12, mackinawite ($Fe_{1+x}S$) formed after initial oxidation of steel. The total sulfide concentration in these investigations ranged from 0.04 M to 0.5 M. The mackinawite film was not completely protective and tended to flake off as it thickened.[8] Iron sulfides are known to increase the corrosion rate of steel. The iron sulfides and their crystal structures are given in Table 1.

Smith and Miller reviewed the effects of various iron sulfide compounds on the corrosion of iron in aqueous solutions.[9] Their review revealed the following:

— Although iron sulfide was thermodynamically predicted to form over a wider range of pH and potential than iron oxide, iron sulfide film was generally not as protective as iron oxide and a more negative cathodic protection potential was required to protect steel in the presence of mackinawite than was generally considered adequate for steel.

— The protectiveness of sulfide scale depended on the sulfide concentration in the aqueous solution and pH. For example, protective pyrrhotite ($Fe_{1-x}S$) scale was reported in the range of 15 ppm to 1,700 ppm whereas nonprotective mackinawite was observed above this concentration and in the pH range of 6.5 to 8.8.

— The corrosiveness of iron sulfide depended on the aqueous solution chemistry. In distilled water saturated with H_2S, a nonprotective mackinawite scale was formed initially but transformed to a protective pyrrhotite and pyrite (FeS_2) scale. In the pres-

ence of brine and CO_2, only a nonprotective mackinawite scale was formed. The corrosion rate continued to increase in the presence of brine.

— In an aqueous solution with iron sulfide suspensions and on an equal molar basis, pyrite was found to be the most corrosive, followed by smythite, greigite (Fe_3S_4), mackinawite, and pyrrhotite. The corrosivity was found to be proportional to the sulfur-to-iron ratio of these compounds (Table 1). It was also found that sulfides produced a strong depolarization of the metal surface, which counteracted the protectiveness of the film. Thus, any defect in the film is likely to enhance the corrosion rate of the steel considerably.

Shoesmith, et al., using galvanostatic tests in aqueous solutions saturated with H_2S, showed that between pH of 4 and 7 the corrosion product consists of mostly mackinawite, and that this layer is protective at first but becomes more porous with time.[10] It was observed that, in these solutions, the potential initially increases corresponding to film formation, then decreases corresponding to disruption, and then stays constant. Huang, et al., observed that saturation of a 4 wt% sodium chloride (NaCl) solution by H_2S resulted in an overall decrease in corrosion rate of A516 (UNS K01880)[(1)] steel, attributable to sulfide precipitation, but increased the corrosion of the ferrite phase because of preferential cathodic reactions on the iron sulfide.[11] A recent investigation has shown that, in the absence of iron sulfide formation, small additions of H_2S (up to 30 mmol) accelerate the dissolution rate of steel.[12] Thus, from the literature, it appears that iron sulfide scales protect corrosion of steel only under a limited set of conditions and that any defect in the film is likely to exacerbate the corrosion considerably.

$CO_2 \pm H_2S$ Corrosion — The earliest studies of the combined effects of CO_2 and H_2S were carried out by Greco and Wright[13] and Sardisco, et al.,[14] who found that a protective sulfide film formed at concentrations of H_2S < 1,700 ppm corresponding to gas pressure of < 0.1 psia. At higher concentrations, a nonprotective sulfide film was reported. Videm and Kvarekval also observed that small concentrations of H_2S (0.02 mmol or 0.0065 psi) decreased the corrosion rate of steel at 70°C and 80°C in a 1 M NaCl solution with 10 psi CO_2.[15] However, pitting occurred in these solutions, possibly caused by selective dissolution of the ferrite phase. At higher H_2S concentrations (0.002 psi to 0.0082 psi), considerable scatter in corrosion rate was observed, with the corrosion rate generally increasing with H_2S concentration. At the natural pH of the H_2S and CO_2 solutions (~ 4), the film formed was not visible and no evidence of sulfides was found. At a pH of 6.9, a thick corrosion product was observed, which consisted of a mixture of FeS, $FeCO_3$, and pyrrhotite. Ho-Chung-Qui and Williamson reported that, in an environment containing H_2S/CO_2 at the ratio of ~ 4, chloride concentration > 10,000 ppm caused severe localized corrosion.[1] The corrosion was associated with the presence of ferrous chloride ($FeCl_2$), which formed as a layer between iron sulfide and the metal.

O_2 Effects — Very few studies of the effect of O_2 have been reported in the literature. Durr and Beavers examined the effect of various O_2 concentrations in a 1,200-psi gas mixture consisting of 1% CO_2 and 3.76 ppm H_2S above a stagnant solution (flowing gas mixture) of 1 wt% NaCl.[16] The corrosion rate was highest at the vapor/liquid interface. The corrosion rate was significant (0.086 mm/y overall corrosion rate and 0.356 mm/y at the vapor/liquid interface) even at the lowest O_2 concentration studied (10 ppm), and there was a gradual increase in penetration with O_2 concentration.

Lyle and Schutt showed that, while formation of iron sulfide films decreased corrosion rates, the sulfide film was not completely protective, as evidenced by localized corrosion.[17] Buffering the solutions to a pH of 6 resulted in a marked decrease in uniform and localized corrosion rate. Chloride increased the localized corrosion rate. Slowly flowing solution increased general corrosion rates and reduced the pitting susceptibility of carbon steel relative to stagnant conditions. Under slowly flowing conditions, the presence of O_2 increased the corrosion rate significantly and enhanced localized corrosion. Specimens were more susceptible to pitting corrosion on portions of partially immersed specimens exposed to the vapor phase. Pitting occurred on fully immersed specimens in only 1 of 11 test conditions, while on the vapor phase portions of partially immersed specimens pitting occurred in 7 of the 11 test conditions. Severe pitting occurred on steel surfaces exposed to the vapor phase when O_2 at a concentration of 100 ppm by volume (ppmv) or 1,000 ppmv was present as the only constituent in the gas being used in the tests. When 0.5 psi H_2S was combined with 100 ppmv or 1,000 ppmv of O_2, severe corrosion of steel surfaces exposed in the vapor phase resulted. In the absence of O_2, 0.5 psi H_2S had little effect on steel corrosion rates. Increasing CO_2 partial pressures tended to increase general corrosion rates of carbon steel and made it more susceptible to pitting, particularly on portions of specimens exposed to the vapor phase. The experimental data of fully immersed specimens yielded a statistical regression equation for general corrosion:

$$CR = 8.7 + 9.86\times10^{-3}(O_2) - 1.48\times10^{-7}(O_2)^2 - 1.31(pH) + 4.93\times10^{-2}(CO_2)(H_2S) - 4.82\times10^{-5}(CO_2)(O_2) - 2.37\times10^{-3}(H_2S)(O_2) - 1.11\times10^{-3}(O_2)(pH) \quad (2)$$

(1) UNS numbers are listed in *Metals and Alloys in the Unified Numbering System*, published by the Society of Automotive Engineers (SAE) and cosponsored by ASTM.

TABLE 2
Chemical Composition of 1018 Carbon Steel used in Corrosion Tests

	Composition (wt%)								
Test Material	C	Mn	P	S	Si	Cr	Cu	Ni	Al
	0.18	0.70	0.005	0.007	0.20	0.01	0.05	0.02	< 0.004

The adjusted regression coefficient (R^2) value for Equation (2) was 0.6235. Equation (2) indicates that O_2 is the most important accelerator of corrosion, that there is a synergistic action between H_2S and CO_2 in increasing corrosion rate, and that increasing pH results in a decrease in corrosion rate. Unlike the DeWaard, et al., equation (Equation [1]), no direct effect of CO_2 partial pressure was found under the conditions examined. Lyle and Schutt conducted one test for a longer period of time (1 month vs the 14 days for all other tests) and found that the general corrosion rates increased with time whereas pitting rate (pit depth divided by total test time) decreased.[17] This would suggest that the corrosion occurred mostly under a nonprotective film and any "localized" corrosion was caused by the nonuniform nature of the corrosion product formed.

Effect of Scale-Forming Species — Some of the corrosion rates measured by Lyle and Schutt were higher than have been experienced by some pipeline operators.[17] This was thought to be caused by the influence of scale-forming species in the pipeline environment. There have been no reported studies of the effects of scale-forming species such as calcium and magnesium on the internal corrosion of pipelines. Although such data are available from field coupon studies, the environmental conditions to which these coupons are exposed are quite variable and complex. The method used to predict precipitation of calcium sulfate ($CaSO_4$) and calcium carbonate ($CaCO_3$) in oilfield waters is based on the experimental approach used by Stiff and Davis.[18-19] For $CaSO_4$, empirical solubility equations were established that modified the solubility of $CaSO_4$ in distilled water through a number of multiplication factors dependent on the concentration of other ions such as sodium and magnesium. For $CaCO_3$, an empirical stability index was established similar to the Langelier index, which corrected for ionic strength, temperature, and alkalinity. These approaches lack a sound theoretical justification and cannot be applied to systems outside the range in which experimental solubility data are available. The experimental studies presented in this paper examine the role of scale-forming species on corrosion in the presence of H_2S and CO_2. A thermodynamic analysis of the system is also presented to better understand the range of conditions possible in these systems.

EXPERIMENTAL PROCEDURES

Cylindrical specimens of Type 1018 carbon steel (UNS G10180) (Table 2) were exposed to stagnant aqueous solutions saturated with gas mixtures containing 0.5 psia H_2S, 10 psia CO_2, and 100 ppmv O_2, in addition to high-purity nitrogen in an amount sufficient to maintain a total pressure of 500 psi. High-purity nitrogen was used instead of methane (CH_4) to reduce the risk of exceeding the flammability limit for O_2-CH_4 gas mixtures. Tests were conducted in stagnant solutions for several reasons: In many gathering and transmission lines, stagnant or slow flow conditions cause high corrosion rates, stagnant conditions tend to maximize the scale-forming tendency, and operational difficulties with the plugging of transfer lines in the laboratory system by scale were encountered. The solution chemistries employed corresponded to the range of Ca^{2+}, Mg^{2+}, Cl^-, and SO_4^{2-} concentrations observed in the field. The test matrix is shown in Table 3. Solution 1 was designed to produce a significant amount of calcium hydroxide ($Ca[OH]_2$) scale by the addition of sodium hydroxide (NaOH) to calcium chloride ($CaCl_2$). In contrast, Solution 2 was slightly undersaturated with respect to $Ca(OH)_2$ and $CaCO_3$. Solution 3 was designed to precipitate magnesium hydroxide ($Mg[OH]_2$) from magnesium chloride ($MgCl_2$). Solution 4 was designed to precipitate $CaSO_4$. Solutions 5, 8, 9, and 10 were control tests to reproduce previous test results as well as further examine the effects of H_2S and O_2. Finally, Solutions 6 and 7 simulated the condensate compositions observed by one gas transmission company. Solution 7 differs from Solution 6 only in terms of a slightly lower pH. The pH of test solutions were calculated after addition of gases containing H_2S and CO_2. The calculations were performed using the Express Calculate module of OLI Systems Environmental Simulation Program (ESP),[†] Versions 5.1 and 6.0. NaOH, in amounts indicated by ESP, was used to make up the pH. As a check on these calculations, the pH was measured prior to the addition of the acid gases and immediately after the test. The measured pH values after the tests are reported in Table 4. There was reasonable agreement between the measured and calculated values.

The test facilities were described fully in a previous paper.[17] Test exposures were conducted simultaneously in 3 L of solution in Type 316L (UNS S31603) stainless steel autoclaves. The temperature within the cell containing the autoclaves was maintained at

[†] Trade name.

TABLE 3
Compositions of Solutions Used in the Experimental Program and their Calculated Scaling Tendencies[A]

Solution Number	Solution Composition	Final pH	Scaling Tendency
1	166 g $CaCl_2$, 58.4 g NaOH, 10 psi CO_2, 0.5 psi H_2S, 100 ppm O_2	11.50	$CaCO_3$: 1.0 $Ca(OH)_2$: 1.0
2	166 g $CaCl_2$, 0.821 g NaOH, 10 psi CO_2, 0.5 psi H_2S, 100 ppm O_2	5.40	$CaCO_3$: 0.146
3	235 g $MgCl_2$, 0.78 g NaOH, 10 psi CO_2, 0.5 psi H_2S 100 ppm O_2	5.10	$MgCO_3$: $1.3 \cdot 10^{-4}$
4	15 g $CaSO_4$, 0.372 g NaOH, 10 psi CO_2, 0.5 psi H_2S, 100 ppm O_2	5.60	$CaSO_4 \cdot 2H_2O$: 1.0
5	30 g NaCl, 1.289 g $NaHCO_3$, 10 psi CO_2, 0.5 psi H_2S, 100 ppm O_2	5.64	No scaling
6	285 g $CaCl_2$, 102 g $MgCl_2$, 7.7 g KCL, 351 g NaCl, 0.639 g NaOH, 10 psi CO_2, 0.5 psi HV, 100 ppm O_2	5.50	Dolomite:1.0
7	285 g $CaCl_2$, 102 g $MgCl_2$, 7.7 g KCl, 351 g NaCl, 0.209 g NaOH, 10 psi CO_2, 0.5 psi HV, 100 ppm O_2	4.80	No scaling
8	30 g NaCl, 0.346 g NaOH, 10 psi CO_2, 0.5 psi HV, zero O_2	5.20	No scaling
9	30 g NaCl, 0.346 g NaOH, 10 psi CO_2, zero O_2	5.12	No scaling
10	0.283 g NaOH, 10 psi CO_2, 0.5 psi HV, zero O_2	4.95	No scaling

[A] All solutions assumed 3,000 mL of solution and the volume of the gas phase was 0.792 L.

15.5 ± 1°C (60 ± 2°F). Premixed gases containing required concentrations of H_2S, CO_2, and O_2 were continuously flowed through liquids in the autoclaves at 10 mL/min. To initiate a test, 189 L (50 gal) of deionized water and the required amounts of NaOH or sodium bicarbonate ($NaHCO_3$) and NaCl were mixed in a glass storage vessel, and the solution was deaerated by evacuating gas from the vessel, followed by sparging high-purity nitrogen through the solution. While the solution in the storage tank was being deaerated, specimens were placed in an autoclave, and the autoclave and the transfer lines between the autoclave, storage tank, and gas bottles were alternately evacuated and back-flushed with high-purity nitrogen to remove air from the system. The solution was then introduced into the autoclave by pressurizing the glass vessel. The system was then pressurized to 500 psi with a premixed gas mixture containing the required partial pressures of H_2S, CO_2, and oxygen in high-purity nitrogen. In each solution, two fully immersed and three partially immersed specimens were exposed. For Solutions 6 and 7, an additional specimen was placed at the bottom of the autoclave to increase the degree of scaling since the precipitates tend to settle to the bottom. All tests were conducted for 14 days. The cylindrical specimens had a surface area of ≈ 9.1 cm^2. Prior to testing, the specimens were degreased and cleaned ultrasonically in a detergent solution, rinsed in alcohol, dried in air, and weighed on an analytical balance accurate to ± 0.1 mg. Average corrosion rates of test specimens were determined from specimen weight-change measurements. The total area of the specimens was used for all cases, although some of the partially immersed specimens showed corrosion only in the immersed portion. For the two specimens placed at the bottom of the autoclave, the area of the threaded holes was also considered.

[2] ASTM, 100 Barr Harbor Drive, West Conshohocken, PA 19428.

Cyclic potentiodynamic polarization curves for a completely immersed specimen were generated using a tungsten/tungsten oxide reference electrode, and the walls of the three autoclaves served as the auxiliary electrodes. The W/WO_3 reference electrode was calibrated against a saturated calomel reference electrode (SCE) prior to the tests in H_2S environments. As shown in Equation (3), the W/WO_3 electrode potential has linear dependence on pH:

$$E(W / WO_3 \text{ vs SCE}) = 0.0271 \cdot pH - 0.039 \qquad (3)$$

However, since most of the solutions were buffered with bicarbonate, the W/WO_3 electrode can be used as a reference electrode. The suitability of the reference electrode was verified by conducting ASTM G-5[2] (potentiodynamic polarization test on Type 430 stainless steel [UNS S43000] in deaerated 1.0 N sulfuric acid [H_2SO_4] at 30°C) and G-61[2] (cyclic potentiodynamic polarization test on Type 304L [UNS S30403] stainless steel in 3.56 wt% NaCl solution at 25°C) tests prior to the tests in CO_2 + H_2S environments.

At the completion of a test and prior to cleaning the specimen, Raman spectroscopy and x-ray diffraction (XRD) analyses were performed on selected specimens to characterize the chemical compositions of deposits formed on specimen surfaces. Specimens were then cathodically cleaned to remove surface deposits in an alkaline cleaning compound (Endox 214†). Tests on unexposed steel specimens have shown that the cleaning procedure causes no measurable change in the weight of uncorroded specimens, and, therefore, has no measurable effect on corrosion rates. After cathodic cleaning, specimens were weighed and examined under a stereoscope for localized corrosion.

Raman spectra were obtained with a Kaiser HoloProbe† system. A 532-nm laser, used as the excitation source, was connected with a fiber optic cable

TABLE 4

Results of Corrosion Tests and Surface Analyses using Raman Spectroscopy

Specimen Number	Test Solution	Final pH	Gas (psi)	Corrosion Rate (mm/y)		Observed Solids	Predicted Solids
				Fully Immersed	Partially Immersed		
1, 2, 3, 4, 5	1	11.5	CO_2 = 10 H_2S = 0.5 N_2 = BAL O_2 (ppmv) = 100	0.068, 0.06	0.11, 0.12, 0.10	$CaCO_3$ $FeCO_3$ β-FeOOH $Fe_{1+x}S$	$CaCO_3$ $Fe_{1+x}S$
6, 7, 8, 9, 10	2	5.4	CO_2 = 10 H_2S = 0.5 N_2 = BAL O_2 (ppmv) = 100	0.19, 0.088	0.067, 0.40, 0.44	$FeCO_3$ β-FeOOH γ-FeOOH	$Fe_{1+x}S$ Very slight tendency to scale by $CaCO_3$ $MgCO_3$
11, 12, 14	3	5.1	CO_2 = 10 H_2S = 0.05 N_2 = BAL O_2 (ppmv) = 100	0.058, 0.035	0.1, 0.045, 0.04	Unassigned Peaks	$Fe_{1+x}S$ Extremely slight tendency to scale by $MgCO_3$
16–20	4	5.6	CO_2 = 10 H_2S = 0.5 N_2 = BAL O_2 (ppmv) = 100	0.147, 0.04	0.046, 0.53, 0.056	$CaSO_4$? $CaCO_2$?	$Fe_{1+x}S$ $CaSO_4$
22, 24	5	5.6	CO_2 = 10 H_2S = 0.5 N_2 = BAL O_2 (ppmv) = 100	0.17, 0.033	0.56, 0.57, 0.33	MCO_3 $MHCO_3$ γ-FeOOH Greigite?	$Fe_{1+x}S$
26, 31	6	4.9	CO_2 = 10 H_2S = 0.5 N_2 = BAL O_2 (ppmv) = 100	0.107, 0.062, 1.3*	0.15, 0.067, 0.054	β-FeOOH γ-FeOOH γ-Fe_2O_2 Dolomite ?	$Fe_{1+x}S$ Dolomite
32, 33, 37	7	4.8	CO_2 = 10 H_2S = 0.5 N_2 = BAL O_2 (ppmv) = 100	0.13, 0.053, 1 47*	0.144, 0.13, 0.11	$Fe_{1+x}S$ β-FeOOH γ-FeOOH	$Fe_{1+x}S$
38, 42	8	5.2	CO_2 = 10 H_2S = 0.5 N_2 = BAL O_2 (ppmv) = 0	0.21, 0.05	0.081, 0.053, 0.068	$Fe_{1+x}S$ γ-FeOOH	$Fe_{1+x}S$
45, 46	9	5.1	CO_2 = 10 H_2S = 0.0 N_2 = BAL O_2 (ppmv) = 0	0.35, 0.35	0.019, 0.043, 0.064	$FeCO_3$ γ-FeOOH	$FeCO_2$
49, 52	10	Final 4.9	CO_2 = 10 H_2S = 0.5 N_2 = BAL O_2 (ppmv) = 0	0.176, 0.12	0.26, 0.11, 0.26	FeS_{1+x} Other peaks unassigned	FeS_{1+x}

to a probe head with a 63.5-mm focal length objective. The laser power was limited to 2.5 mW in order to minimize fluorescence and prevent oxidation of the corrosion products. Exposure time for each spectrum accumulation varied but was limited to a maximum of 240 s. Typically, at least two accumulations were used to obtain the Raman spectra of the specimens. Test specimens were placed in a V-block mounted on an X-Y μm stage with a 50-mm travel and 0.01-mm resolution, and Raman spectra were obtained on at least two locations along the length of the specimens. Additional spectra were collected for specimens where multiple corrosion products appeared to be present. The spectra from standard compounds were compared in order to identify the corrosion products formed. The spectra of standard compounds are shown in Appendix A. Selected specimens were also analyzed by XRD using a Siemens D-500† x-ray

diffractometer with Cu K-alpha radiation. The diffractometer was operated at 40 kV with a current of 30 mA. XRD analyses of the corrosion products agreed with the Raman analyses.

THERMODYNAMIC ANALYSIS

The Corrosion Simulation Program (CSP), developed by OLI Systems† was used to find the equilibrium speciation of complex fluids and, thus, predict the occurrence of scale-forming compounds and corrosion products. The equilibrium computations are based on a comprehensive thermodynamic model, which is applicable to aqueous systems of virtually any complexity.[20,24-25] The most common sparingly soluble compounds that may deposit on the metal surface in scale-forming solutions containing Ca^{2+} are calcium carbonate and calcium sulfate. However, various calcium, magnesium carbonates may also precipitate in multicomponent aqueous solutions (e.g., $CaMg[CO_3]_2$ and $CaMg_3[CO_3]_4$ in the presence of magnesium ions). Stiff and Davis developed a technique for predicting the solubility of $CaCO_3$ and $CaSO_4$ in natural brines.[18-19] However, the method is not based on rigorous thermodynamic analysis, employs arbitrary assumptions (e.g. the independent character of the common ion, sodium, and magnesium factors), and is not designed for systems with multiple ions and neutral species. To predict the equilibrium solid and dissolved species from corrosion reactions, two kinds of stability diagrams are available in CSP: Electrochemical diagrams (i.e., those utilizing the potential [E] and pH or concentrations of aqueous species as independent variables) are extensions of the classical Pourbaix diagrams to real (e.g., concentrated) solutions and offer a flexible choice of independent variables.[24-25] These diagrams make it possible to analyze various combinations of redox processes on metal surfaces that may lead to the formation of potentially protective films or to the dissolution of metals. In the second type of diagram, chemical diagrams (i.e., those utilizing concentrations or various species and/or temperature as independent variables), the potential is not an independent variable, but results from the solution of chemical and phase equilibria in the system of interest. These diagrams show the most stable species in the system and, thus, represent the global equilibrium of the system. These diagrams have been described by Lencka, et al.[26]

In all cases, it was assumed that the amount of the gas phase is 100 moles/kg of solution. This assumption is somewhat arbitrary and is intended to satisfy the condition that the gas phase be sufficiently large so that the composition of the gas is not changed as a result of the dissolution of CO_2 and H_2S in the aqueous phase and the subsequent reaction with iron. Thus, 0.5 psi H_2S in a total gas pressure of 500 psi corresponds to 0.1 moles/kg of solution. The volume of gas phase in the experiments at any time is 0.79 L. Assuming ideal gas behavior, the number of moles of gas introduced during the course of the test (336 h) at a gas flow rate of 10 mL/min is ~ 290 moles for 3 L of solution. Therefore, the total amount of gas may be considered to be 100 moles/kg of solution. In pipelines, the gas volume-to-solution ratio may be considerably larger than in laboratory autoclave tests.

RESULTS

Prediction of Scaling Tendency and Corrosion Products

Scale in this paper is distinguished from corrosion products as resulting mainly from the chemical reactions occurring in the solution without the presence of cationic species from the metal dissolution. The detailed stability diagrams are presented elsewhere[21] and the results are as follows:

— The formation of calcium- and magnesium-containing scales is predicted to be independent of the formation of iron sulfides.

— The stability of the potentially protective scales is primarily determined by pH. Only $CaSO_4 \times 2H_2O$ can be stable under acidic conditions. Carbonates become stable for pH values ranging from 5.5 to 8 for realistic CO_2 concentrations. The value of pH for initiating the precipitation of carbonates depends on the concentration of CO_2.

— There is a synergy between calcium and magnesium ions in the precipitation of carbonates. The mixed calcium/magnesium carbonate can be stable at somewhat lower pH values than the carbonates that contain only calcium or magnesium.

— To facilitate the analysis of data in a wide variety of environmental conditions, it is convenient to use solid scaling tendencies because they indicate how close a given environmental condition is to the precipitation of a given solid. If a separate solid phase "B" precipitates according to the following reaction:

$$B = \sum_i A_i \qquad (4)$$

its scaling tendency is defined as:

$$s = \frac{\prod_i a_i}{K_B} \qquad (5)$$

where a_i is the activity of the A_i species and K_B is the equilibrium constant for the reaction shown in Equation (4). When the solid B is in equilibrium with the aqueous phase, the scaling tendency is equal to 1. If one of the A_i species is absent in the solution, the

scaling tendency with respect to that species is equal to 0. In an unsaturated solution, the scaling tendency varies from 0 to 1. If the scaling tendency is high (e.g., > 0.8 or even 0.5), a relatively small variation in the solution composition may cause the precipitation of the solid. For scaling tendencies close to 1, the corrosion rates should be smaller provided that the scale is protective. A comparison of the anticipated precipitation and the precipitates observed by Raman spectroscopy and XRD are shown in Table 4. Generally, there was agreement between predicted and observed scale and corrosion products.

Four phases—β-FeOOH, $FeCO_3$, mackinawite, and $CaCO_3$—were detected on Specimens 1 to 5, and most of the spectra were consistent with β-FeOOH. Identification of $FeCO_3$ and $CaCO_3$ was made by the location of the 280 cm^{-1} peak ($CaCO_3$) and the 296 cm^{-1} and 508 cm^{-1} peaks ($FeCO_3$). The small 2,171 cm^{-1} peak indicated that a minor amount of mackinawite was present in the corrosion products. These results agree with the predicted scaling tendency of 1 with respect to $CaCO_3$, but $Ca(OH)_2$ was not observed in the Raman spectra. It is possible that $Ca(OH)_2$ is kinetically hindered or not easily distinguishable from the O-H stretch peak of water. For test Specimens 6 to 10 tested in 0.50 M $CaCl_2 \cdot 2H_2O$ + 0.007 M NaOH, β-FeOOH was the most prevalent phase found in the corrosion products. Some indication of γ-FeOOH was also found based on the 248 cm^{-1} peak. While no mackinawite was found, a significant amount of $FeCO_3$ was observed in the spectra of corrosion products from these specimens. No calcium scale was found. This corresponds reasonably well with the low tendency predicted for the scaling of $CaCO_3$ for this solution. Raman spectra for Specimens 11 to 15 tested in 0.82 M $MgCl_2 \cdot 6H_2O$ + 0.007 M NaOH showed a large 3,420 cm^{-1} peak that can be attributed to water on the specimen surface from the test solution. All of the spectra have a very strong peak at 289 cm^{-1} to 293 cm^{-1}, which cannot be attributed to either water or any of the possible corrosion products or mineral phases that would be expected to precipitate from the solution. The very slight scale-forming tendency predicted for this solution is in agreement with the lack of observable scale in this solution.

The Raman spectra of corrosion products from Specimens 16 to 20, tested in 0.035 M $CaSO_4 \cdot 2H_2O$ + 0.003 M NaOH, clearly indicated the presence of a mixture of $CaSO_4$ and $CaCO_3$, in agreement with predicted scaling of $CaSO_4$. Specimens tested in 0.17 M NaCl + 0.005 M $NaHCO_3$ were found to have mainly γ-FeOOH and lesser amounts of β-FeOOH. Another phase was also present that had Raman peaks at 298 cm^{-1} and 352 cm^{-1} and a broad peak at 675 cm^{-1}. These peaks are not consistent with the presence of $NaHCO_3$ or any of the possible iron corrosion products. These peaks may correspond to Fe_3S_4. For example, the peak at 352 cm^{-1} is similar to the 347 cm^{-1} peak found for other iron sulfides. Nakamoto cites several investigations of sulfate-reducing bacterial proteins which have terminal Fe-S stretching frequencies in the 352 cm^{-1} region.[28] Corrosion products consisting of β-FeOOH and γ-FeOOH were also found on Specimens 26 and 31 tested in Solution 6, containing 0.86 M $CaCl_2 \cdot 2H_2O$, 0.36 M $MgCl_2 \cdot 6H_2O$, 0.034 M KCl, 2.00 M NaCl, and 0.005 NaOH. Although the peak at ~ 300 cm^{-1} may arise from dolomite ($CaMg[CO_3]_2$), other characteristic Raman peaks for $CaMg(CO_3)_2$ were absent. The presence of $CaMg(CO_3)_2$ would be in general agreement with the predicted formation of $CaMg(CO_3)_2$ in this solution. When the concentration of NaOH was reduced to 0.0016 M (Solution 7), mackinawite was found in the corrosion product layers, in addition to β-FeOOH and γ-FeOOH. No scaling was noted, in agreement with thermodynamic prediction.

Raman spectra for specimens tested in 0.17 M NaCl + 0.003 M NaOH indicate only the presence of mackinawite and β-FeOOH. The relatively weak spectra for mackinawite likely indicates that only a small amount of mackinawite was formed in the corrosion product layers. The Raman spectra of specimens from a subsequent test performed without H_2S in the system (Solution 9) indicates that the corrosion products contain both γ-FeOOH and $FeCO_3$. The unique peak for $FeCO_3$, located at 508 cm^{-1}, is quite weak in this spectra, especially compared to the same peak in Solution 2 containing $CaCl_2$. Because of the strong 1,080 cm^{-1} carbonate peak, this may indicate that other carbonate species are forming in the corrosion product layer. Based on the solution composition, sodium carbonate (Na_2CO_3) would be the only other carbonate species to form in this test, but it is unlikely given the near-neutral pH. Raman spectra for specimens tested in 0.0023 M NaOH (Solution 10) show strong peaks at 300 cm^{-1} and 356 cm^{-1}. These peaks cannot be assigned to any of the corrosion products or mineral phases examined previously. Other minor peaks located at 2,171, 2,820, 3,414, and 3,692 cm^{-1} can be assigned to mackinawite.

The corrosion rates are shown in Table 4. In analyzing the corrosion behavior, results from a previous program were also considered.[17] The weight-loss corrosion rate is plotted against scaling tendencies of the laboratory test solutions (Table 3) in Figures 1 and 2 for fully and partially immersed samples, respectively. There appears to be no correlation between the calculated scaling tendency and the corrosion rate.

Effect of pH

As shown in Equation (2), increasing the pH resulted in a decrease in corrosion. This is illustrated in Figure 3, which shows that the corrosion rate in

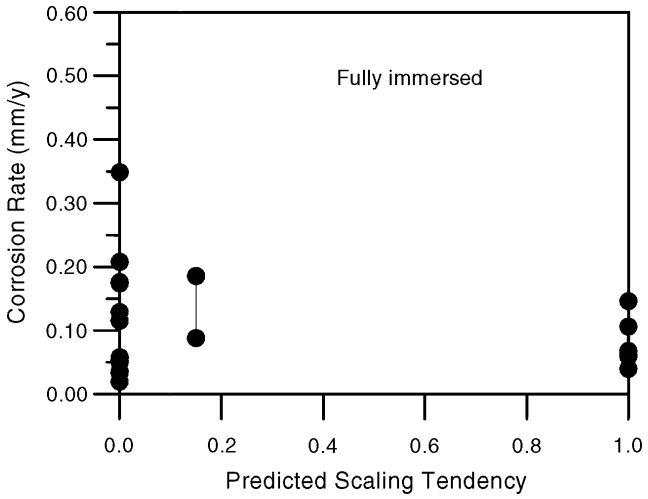

FIGURE 1. *Effect of scaling, as predicted by scaling tendency on corrosion rates of fully immersed specimens.*

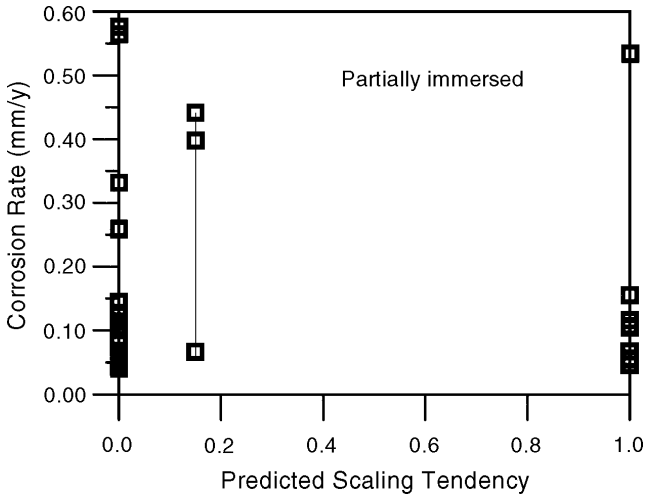

FIGURE 2. *Effect of scaling on measured corrosion rates of partially immersed specimens.*

chloride-free solutions under a variety of gas mixtures was generally lower when the pH was increased to ~ 6. The test conducted at pH 11.5 had a solution with 3.53 wt% chloride. The large scatter in the data makes an unequivocal conclusion of the role of pH on corrosion difficult and may well be related to the dual role of sulfide films in protecting and enhancing the corrosion of steel.

Effect of Chloride Concentration

The corrosion rate in various chloride solutions, under a gas mixture of CO_2 + H_2S + O_2, increased with small additions of chloride but was insensitive to larger concentrations. This is illustrated further in Figure 4 where the average corrosion rates of fully immersed and partially immersed specimens are plotted as a function of chloride concentration. However, at concentrations > 5%, localized corrosion was observed.

Polarization Behavior of Steel

A typical cyclic potentiodynamic polarization curve is shown in Figure 5, indicating a completely active behavior. In the H_2S environment, the increase in polarization at high current densities is essentially the result of transport-limited dissolution rather than protective film formation or a large ohmic component. The potential-current density relationship is not linear, and there is a slight hysteresis in the polarization behavior. The transport-limiting process was not determined in this study, but could be the diffusion of dissolved ferrous hydrogen sulfide ($Fe[HS]^+$) complexes away from the electrode. The lack of passivity is evident not only in the shape of the polarization curves, but also in the lack of significant hysteresis between the forward and backward scans. Typically, if passive films exist and localized corrosion is observed, significant hysteresis in the

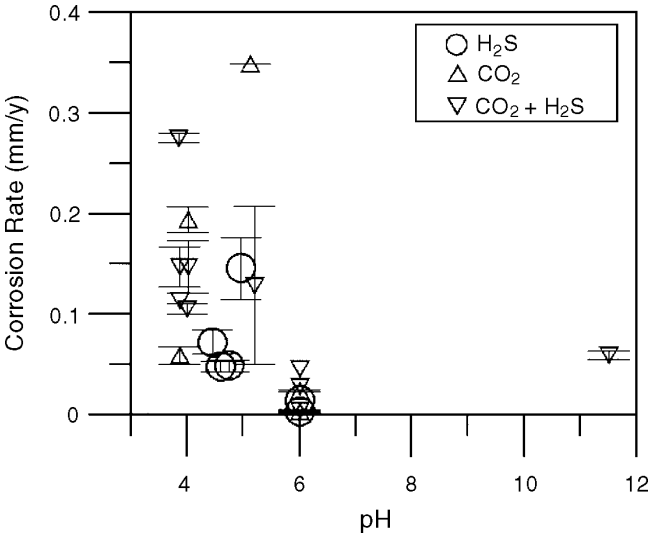

FIGURE 3. *Effect of pH on general corrosion rate of completely immersed specimens.*

polarization curves will occur. The lack of passive behavior indicates that the scale or corrosion products formed on the steel may have provided minimal protection. The presence of oxygen in the gas phase increases the corrosion potential significantly, as shown in Figure 6. This indicates that O_2 promotes corrosion through cathodic depolarization.

DISCUSSION

The lack of observed correlation between measured corrosion rates and predicted scaling tendency may be attributable to the scale being nonprotective or only partially covering the surface. It is possible that most of the precipitation occurred on the bottom of the autoclave rather than on the specimens. However, the specimens on the floor of the autoclave in

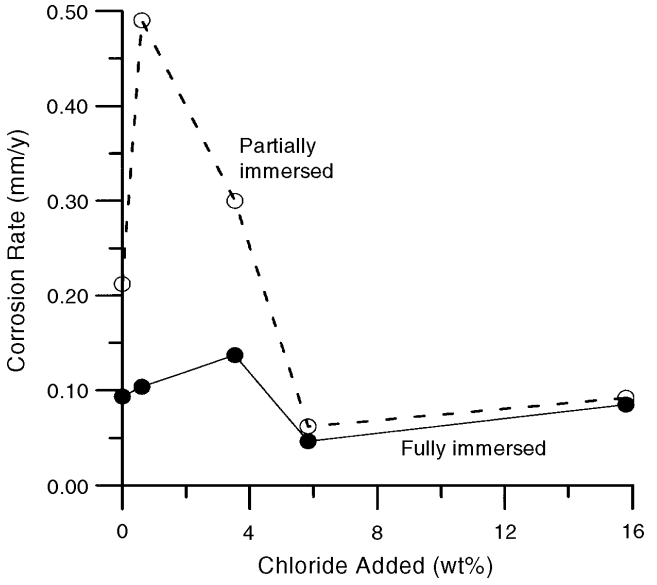

FIGURE 4. *Effect of chloride concentration on general corrosion rate.*

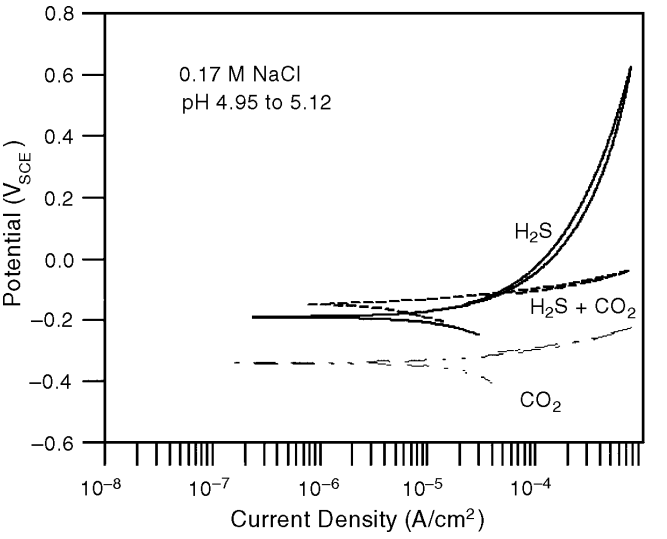

FIGURE 5. *Cyclic potentiodynamic polarization curves for steel in various environments. Scan rate: 0.167 mV/s.*

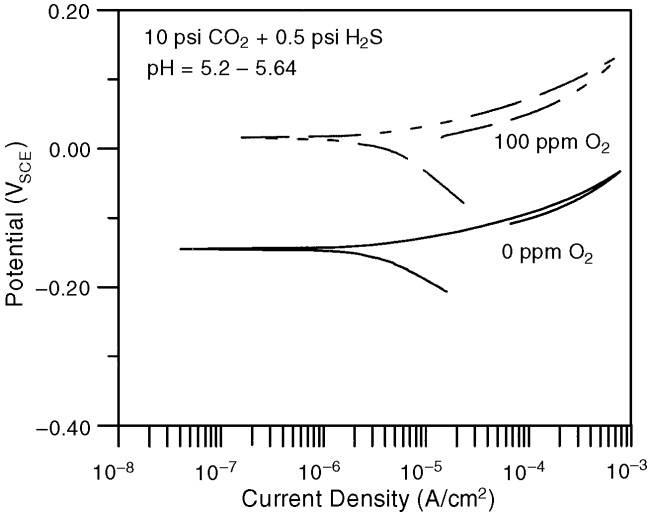

FIGURE 6. *Cyclic potentiodynamic polarization curves for steel vs oxygen concentration in the gas. Scan rate: 0.167 mV/s.*

Solutions 6 and 7 did not exhibit lower corrosion rate than the fully or partially immersed specimens. Indeed, these specimens showed considerably higher corrosion rates (1.3 mm/y in Solution 6 and 1.47 mm/y in Solution 7 for floor specimens vs 0.085 mm/y and 0.09 mm/y for fully immersed specimens in the same solutions). It is possible that the floor specimens generated greater amounts of iron sulfides locally, which acted as cathodic depolarizers and increased the corrosion rates. The test time also may not have been sufficiently long to differentiate the corrosion rates between scaling and nonscaling solutions. The range of corrosion rates under scale-forming conditions was generally narrower, with the exception of one partially immersed specimen. This would suggest that a larger sample size and variations in geometry of exposure may be necessary to determine the effect of scaling on corrosion more accurately.

Empirical models developed through limited tests are not valid beyond the range of factors used to develop the models. Thus, the DeWaard, et al., model (Equation [1]) cannot be used in environments containing H_2S in addition to CO_2. By the same token, the empirical model developed by Lyle and Schutt (Equation [2]) cannot be used in an environment without H_2S and O_2 because the model does not indicate a dependence on CO_2 alone. The objective of this paper is not to develop a comprehensive model containing any or all three gaseous species, but to provide an understanding of the factors that could influence the corrosion behavior in the presence of these gases.

While thermodynamic models cannot explain the corrosion kinetics, the environmental conditions under which corrosion products can precipitate may be examined. Whether these corrosion products are protective or not can be examined by kinetic measurements and models. FeS_2 and FeS (troilite or stoichiometric pyrrhotite) are the most stable iron sulfide forms. However, it is known that they do not form as the initial corrosion products. For example, FeS_2 is stable under mildly acidic conditions, but its precipitation is kinetically inhibited.[22-23] It has been shown[24-25] that stability diagrams can be used to study the formation of metastable species in addition to stable ones. The E-pH diagram in Figure 7 has been generated by considering the metastable iron sulfide species. The dashed lines indicate the stability fields of various aqueous complexes, while the solid lines indicate the stability fields of the solid

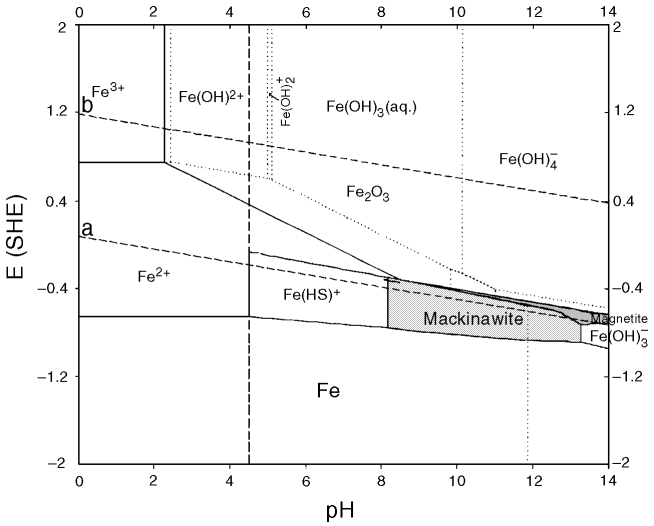

FIGURE 7. *E-pH diagram of a system containing 0.5 psi H_2S and 10^{-6} M dissolved iron, considering only metastable iron sulfide species.*

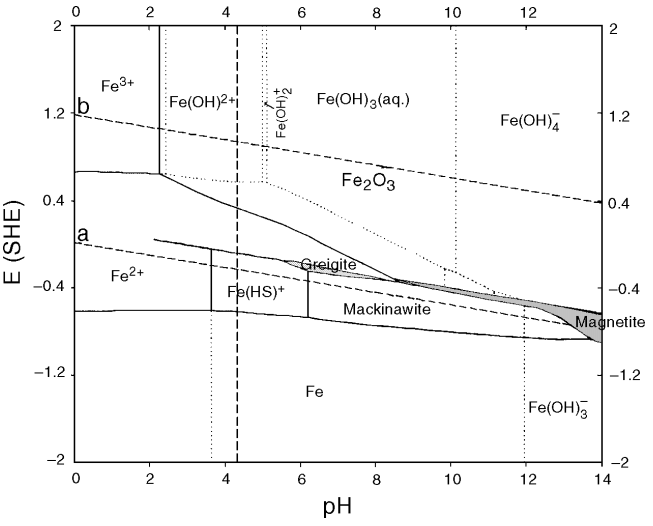

FIGURE 8. *E-pH diagram of a system containing 0.5 psi H_2S and 10^{-4} M dissolved iron.*

phases. The dashed vertical line at ≈ pH 4.5 indicates the equilibrium pH predicted for this environment. Mackinawite is the metastable solid that is likely to form as a corrosion product. However, the stability field of mackinawite starts at pH > ≈ 8. Thus, the system is predicted to be in the range of active dissolution as shown by the vertical dotted line, at a pH of ~ 4.5.

The stability fields of metastable Fe-S species are affected by the partial pressure of H_2S and the amount of iron dissolved in the aqueous phase. Since the experiments were performed in a stagnant solution, a buildup of corrosion products could be expected in the vessel. This should have increased the amount of dissolved iron that was available for the formation of mackinawite. Figure 8 shows the same E-pH diagram for an assumed dissolved iron concentration of 10^{-4} M. It can be seen that the mackinawite stability region has shifted to lower pH values (≈ 6). The addition of 10 psi CO_2 results in the appearance of a small region of $FeCO_3$, as shown in Figure 9.

Because the stability of mackinawite is influenced by both the H_2S and dissolved iron concentrations, a different kind of stability diagram has been constructed to investigate the effects of these species in an explicit way. Figure 10 shows a stability diagram with the molality of iron in the aqueous phase as an x-axis variable. The y-axis shows the amount of H_2S added to the solution per 1 kg of water on the assumption that the vapor phase contains 100 moles of neutral gases. The latter assumption was arbitrary and was consistent with the requirement that the amount of the vapor phase be large so that its composition does not change. An important result, observable in Figure 10, is the dependence of the stability field of mackinawite on the amounts of both

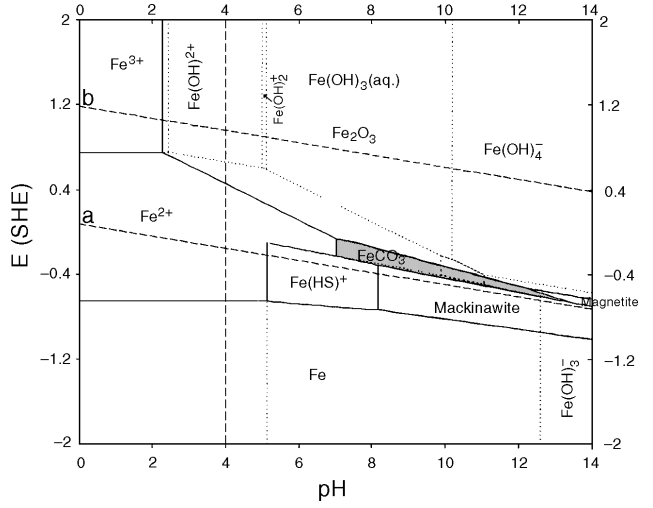

FIGURE 9. *Effect of 10 psi CO_2 on the stability fields of iron in water and 0.5 psi H_2S at 15.5°C. A dissolved concentration of 10^{-6} moles/kg iron is assumed.*

H_2S and dissolved iron. If a sufficient gas phase is present, the amount of dissolved iron required to form mackinawite may be quite significant. For the experimental condition of 0.5 psia H_2S (10^{-1} moles/kg) mackinawite starts to appear when the amount of dissolved iron is roughly ~ $10^{-4.1}$ (or 7.9×10^{-5}) M. In the absence of H_2S, iron oxides are predicted to form (Figure 10). In the laboratory experiments, iron oxyhydroxides, FeOOH, form prior to the formation of magnetite (Fe_3O_4). The amount of iron required to form mackinawite is greater when CO_2 is present in the system (Figure 11). Another interesting observation is the boundary between $FeCO_3$ and mackinawite. This boundary shows how much H_2S is necessary to form mackinawite in the presence of CO_2. The limit-

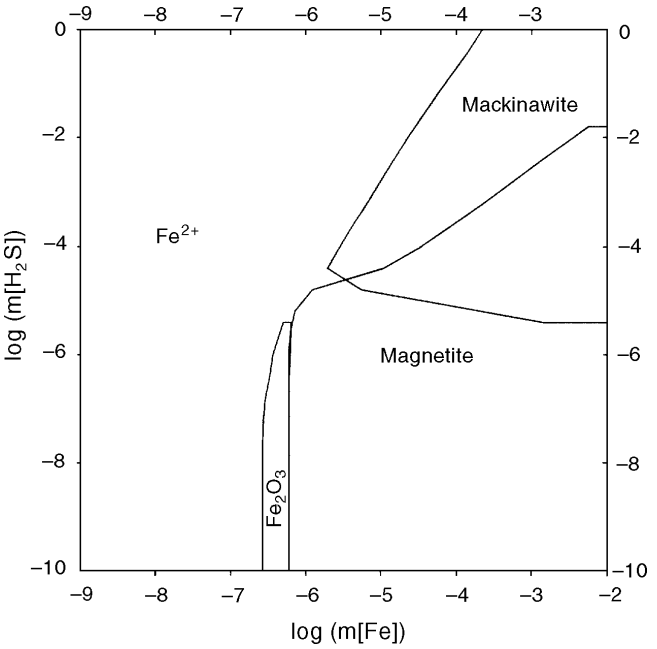

FIGURE 10. *Stability diagram as a function of molality of dissolved iron and the number of moles of H_2S per 1 kg of H_2O and 100 mol of neutral gas phase.*

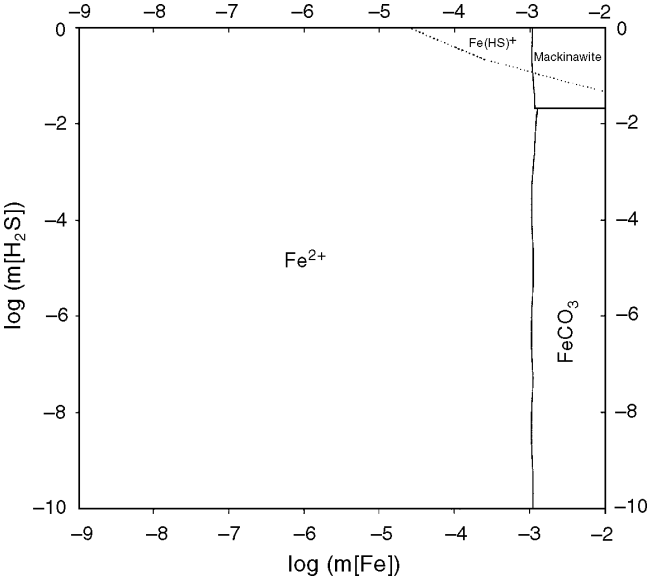

FIGURE 11. *Stability diagram for a system containing 10 psi CO_2. Other conditions are as in Figure 10.*

ing partial pressure of H_2S for mackinawite in a CO_2-containing system is ≈ 0.1 psia ($10^{-1.67}$ moles/kg), which is fairly low. Since the literature indicates that large amounts of mackinawite precipitation is not likely to be protective,[9] prediction of mackinawite formation alone is not sufficient to determine the corrosion rate.

The stability diagram for a system containing 0.5 psia H_2S as a function of the amount of dissolved iron and O_2 added to the vapor phase is shown in Figure 12. For the gas phase containing 100 moles of neutral gas, 10^{-1} moles/kg O_2 on the vertical axis corresponds to 1,000 ppmv O_2, 10^{-2} moles/kg corresponds to 100 ppmv, etc. As shown in Figure 12, the increase in the amount of oxygen results first in the conversion of mackinawite into Fe_3S_4. This starts at 1 ppmv O_2 (10^{-4} moles/kg on the vertical scale). The boundary between mackinawite and Fe_3S_4 depends on the amount of dissolved iron. However, mackinawite disappears for O_2 amounts > ≈ 5,000 ppmv for reasonable amounts of dissolved iron. A further increase in the amount of O_2 results in the dissolution of Fe_3S_4 and a shift of the state of the system to the active dissolution range. Similar to Figures 10 and 11, addition of CO_2 resulted in iron sulfide stability fields shifting to a higher dissolved iron concentration.

Lyle and Shutt reported the effect of slowly flowing solution on the corrosion rate in O_2-containing systems.[17] If the solution is slowly flowing, buildup of corrosion products in the vessels is minimized. Therefore, simulations were performed by assuming that the concentration of the aqueous phase remains virtually unchanged. In particular, the pH of the solution can be assumed to be constant rather than to vary with the amount of dissolved iron. Thus, the stability diagrams have been regenerated using pH and O_2 concentration as independent variables and the amount of dissolved iron as a parameter, as exemplified by Figure 13. In this case, the effect of pH and O_2 in a system containing 10^{-4} m Fe, 0.5 psi H_2S, and 10 psi CO_2 is shown. The Fe_3S_4 and mackinawite incipient precipitation lines are observed at a pH slightly > 6.

The thermodynamic simulation can assist experimental studies in identifying regions where precipitation of specific corrosion products can occur. However, a thermodynamic model alone cannot predict changes in corrosion rates. The polarization curves indicate that the dissolution behavior of the steel in these environments does not exhibit any passivity. Thus any reduction in corrosion rate observed in weight-loss experiments is essentially attributable to a barrier layer of precipitate blocking access of the electrolyte to the metal. However, if this barrier layer is porous, the presence of iron sulfides, such as mackinawite and Fe_3S_4, can increase the corrosion rate of steel by providing sites for enhanced cathodic reduction reaction. The corrosion potential increases by ~ 200 mV in the presence of H_2S (Figure 5). Since the pH of the solution was buffered by the presence of bicarbonate (Table 4), the increase in potential is not likely to have been caused by the change in the reference potential of the W/WO_3 electrode (Equation [3]). The increase in corrosion potential may be explained by the presence of iron sulfides increasing the cathodic reaction kinetics or the effect of H_2S on

the hydrogen evolution reaction. The addition of CO_2 and H_2S increases the anodic reaction kinetics even further without a significant shift in the corrosion potential. This is consistent with the thermodynamic speciation model which suggests that addition of CO_2 results in a shift of the mackinawite stability field to higher iron concentrations, thus reducing the blocking effect of iron sulfides. However, since the corrosion potential is increased even in the presence of CO_2, the mechanism for the increase in corrosion potential is not likely to be the catalytic effect of iron sulfides. The observed increase in anodic kinetics in the combined presence of H_2S and CO_2 (Figure 5) is also consistent with the regression equation (Equation [2]) derived from weight-loss measurements.

As seen in Figure 6, the presence of O_2 results in an increase in corrosion potential. Raman spectroscopy did not reveal the presence of any elemental sulfur, and hence the increase in corrosion potential is essentially attributable to the additional cathodic reduction reaction of O_2. The higher corrosion in the partially immersed specimen (Table 4) points to the greater availability of O_2 in the vapor/liquid interface. It has also been speculated that the change in crystal structure from mackinawite to Fe_3S_4 promotes disruption of the protective sulfide and increased localized corrosion.[27]

CONCLUSIONS

❖ The internal corrosion behavior of steel pipeline in condensate environment was studied using thermodynamic modeling and experimental techniques. The important conclusions of this study can be summarized as follows:

❖ No significant correlation between calcium and magnesium scaling tendency and corrosion rate in the presence of Cl^-, CO_2, H_2S, and O_2 was observed. This may be because the scales formed did not provide adequate protection or did not form in sufficient amounts. A similar conclusion was reached by analyzing the results of field corrosion coupons. Thermodynamic modeling provides a convenient tool to characterize the water chemistry in terms of its scaling tendency.

❖ Iron sulfide offers poor protection to the steel and can enhance corrosion by acting as a cathodic depolarizer. This finding was supported by electrochemical polarization tests, which showed an essentially active corrosion, without any passivity afforded by the corrosion product films and an increase in corrosion potential in H_2S environments.

❖ The corrosion rate measurements were also consistent with the anodic polarization behavior of steel, which showed a significant increase in corrosion potential in the presence of H_2S in the gas phase and an increase in anodic currents in the combined presence of CO_2 and H_2S.

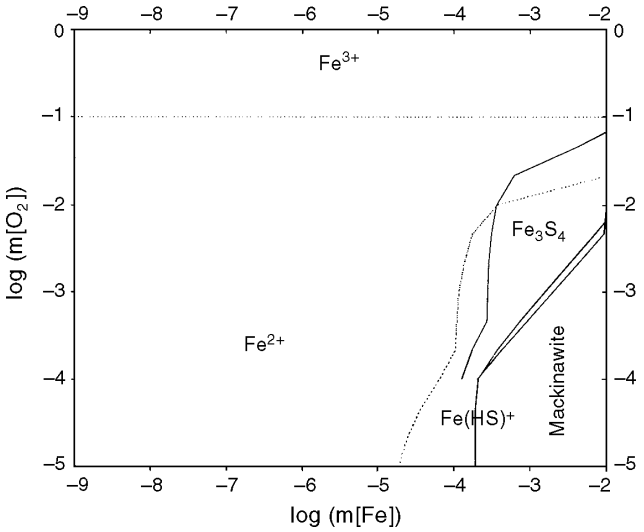

FIGURE 12. *Stability diagram for a system containing 0.5 psi H_2S as a function of iron and O_2 concentrations.*

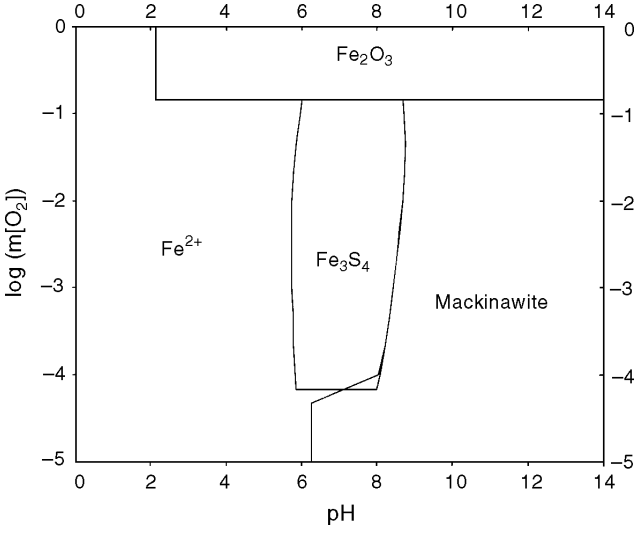

FIGURE 13. *Stability diagram for a system containing 10^{-4} moles/kg dissolved iron and 10 psi CO_2 as a function of pH and H_2S concentration.*

❖ The corrosion rate of partially immersed specimens was higher than that of fully immersed specimens. This may be related to the easier access of O_2 to the surface or the effect of corrosion products such as greigite in enhancing cathodic reaction kinetics.

❖ The comprehensive thermodynamic modeling applied to the internal corrosion environment provides a useful tool to examine the corrosion behavior in a complex environment in terms of the stability of various precipitated compounds. The model predictions were in general agreement with surface analytical results by Raman spectroscopy. Further development of standard Raman spectra may help confirm the presence of certain compounds predicted by the model and suspected to be present.

❖ In addition to the thermodynamic predictions of the regions of phase stability, the morphology, electrochemical kinetics of anodic and cathodic reactions, and possible deleterious effects of precipitated compounds such as mackinawite and Fe_3S_4 need to be considered in evaluating the effects of environment on corrosion.

ACKNOWLEDGMENTS

The authors acknowledge the contributions and support of various Southwest Research Institute staff members in carrying out the activities described in this report: V.D. Aaron, J.L. Sievert, and S.T. Clay, who were responsible for the day-to-day conduct of laboratory corrosion exposures; M. Bogart and J.F. Spencer, who performed the Raman spectroscopy and x-ray diffraction studies, respectively; and G. Cragnolino, O. Moghissi, and F.F. Lyle, who provided valuable advice during the project. This work was funded by PRCI under the project number PR-15-9712. The opinions, findings, and conclusions expressed are those of the authors and not necessarily those of the PRCI. Mention of company or product names is not to be considered an endorsement by PRCI or SwRI.

REFERENCES

1. D.F. Ho-Chung-Qui, A.I. Williamson, "Pipeline Corrosion—H_2S and O_2 Corrosion of Pipelines," Corrosion Information Compilation Series (Houston, TX: NACE International, 1999), p. 41.
2. N.N. Bich, K. Goerz, Pipeline Gas J. (1997): p. 46-48.
3. F.F. Lyle, H.C. Burghard, Jr., E.P. George, "Effect of Natural Gas Quality on Corrosion of CNG Storage Cylinders—Phase I," Report No. 90-13, Project No. 730-FFES-FUC-85 (Albany, NY: New York State Energy Development Authority, 1990).
4. C. de Waard, D.E. Milliams. 1975. "Prediction of Carbonic Acid Corrosion in Natural Gas Pipelines," in CO_2 Corrosion in Oil and Gas Production (Houston, TX: NACE, 1984), p. 506-510.
5. C. de Waard, U. Lotz, A. Dugstad, "Influence of Liquid Flow Velocity on CO_2 Corrosion: A Semi-Empirical Model," CORROSION/95, paper no. 128 (Houston, TX: NACE, 1995).
6. C.A. Palacios, Y. Hernandez, "Application of Simulation Techniques for Internal Corrosion Prediction," CORROSION/97, paper no. 2 (Houston, TX: NACE, 1997).
7. D.W. Shoesmith, P. Taylor, M.G. Bailey, B. Ikeda, Electrochem. Acta 23 (1978a): p. 903-916.
8. D.W. Shoesmith, M.G. Bailey, B. Ikeda, Electrochem. Acta 23 (1978b): p. 1,329-1,339.
9. J.S. Smith, J.D.A. Miller, Brit. Corros. J. 10, 3 (1975): p. 136-143.
10. D.W. Shoesmith, P. Taylor, M.G. Bailey, D. Owen, J. Electrochem. Soc. 127 (1980): p. 1,007-1,015.
11. H.H. Huang, W.T. Tsai, J.T. Lee, Corrosion 52, 9 (1996): p. 708-713.
12. X.L. Cheng, H.Y. Ma, J.P. Zhang, X. Chen, S.H. Chen, H.Q. Yang, Corrosion 54, 5 (1998): p. 369-376.
13. E.C. Greco, W.B. Wright, Corrosion 18 (1962): p. 119t-124t.
14. J.B. Sardisco, W.B. Wright, E.C. Greco, Corrosion 19 (1963): p. 354t.
15. K. Videm, I. Kvarekval, Corrosion 51, 4 (1995): p. 260-269.
16. C.L. Durr, J.A. Beavers, "Effect of Oxygen on the Internal Corrosion of Natural Gas Pipelines," CORROSION/96, paper no. 612 (Houston, TX: NACE, 1996).
17. F.F. Lyle, H.U. Schutt, "CO_2/H_2S Corrosion Under Wet Gas Pipeline Conditions in the Presence of Bicarbonate, Chloride, and Oxygen," CORROSION/98, paper no. 11 (Houston, TX: NACE, 1998).
18. H. Stiff, L.E. Davis, "A Method for Predicting the Tendency of Oilfield Waters to Deposit Calcium Sulfate," Petroleum Transactions. American Institute of Mechanical Engineering, 195 (1952a): p. 25-28.
19. H. Stiff, L.E. Davis, "A Method for Predicting the Tendency of Oilfield Waters to Deposit Calcium Carbonate," Petroleum Transactions. American Institute of Mechanical Engineering, 195 (1952a): p. 213-216.
20. M. Rafal, J.W. Berthold, N.C. Scrivner, S.L. Grise, "Models for Electrolyte Solutions," in Models for Thermodynamic and Phase Equilibria Calculations, ed. S.I. Sandler (New York, NY: Marcel Dekker, 1995), p. 601-607.
21. N. Sridhar, D.S. Dunn, A. Anderko, M. Lencka, "The Effects of Water Chemistry on Internal Corrosion of Steel Pipelines," Final Report PR-15-9712 (Arlington, VA: Pipeline Research Committee International, 1998).
22. M.A.A. Schoonen, H.L. Barnes, Cosmochim. Acta 55, 6 (1991): p. 1,495-1,504.
23. M.A.A. Schoonen, H.L. Barnes, Geochim. Cosmochim. Acta 55, 6 (1991): p. 1,505-1,514.
24. A. Anderko, P.J. Shuler, Comput. Geosci. 23 (1997): p. 647-658.
25. A. Anderko, S.J. Sanders, R.D. Young, Corrosion 53, 1 (1997): p. 43-53.
26. M.M. Lencka, E. Nielson, A. Anderko, R.E. Rieman, Chemistry of Materials 9 (1997): p. 1,116-1,125.
27. M.B. McNeil, B.J. Little, Corrosion 46, 7 (1990): p. 599-600.
28. K. Nakamoto, Infrared and Raman Spectra of Inorganic and Coordination Compounds (New York, NY: John Wiley, 1978).
29. D.S. Dunn, M.B. Bogart, C.S. Brossia, G.A. Cragnolino, "Corrosion of Iron Under Alternating Wet and Dry Conditions," CORROSION/99, paper no. 223 (Houston, TX: NACE, 1999).

APPENDIX A

Raman Spectra of Standard Compounds

The Raman spectra for iron oxides and hydroxides have been reported elsewhere.[29] Corrosion products formed on iron exposed to aqueous chloride solutions typically contain γ-FeOOH, β-FeOOH, Fe_3O_4, and γ-Fe_2O_3. For most of these compounds, the Raman spectra can be used to identify the phases present. It is often difficult to identify the formation of Fe_3O_4 when γ-FeOOH, β-FeOOH, or γ-Fe_2O_3 are present due overlapping peaks hiding the relatively weak 667 cm^{-1} peak for Fe_3O_4. For γ-FeOOH, the strong peaks at 248 cm^{-1} and 1,311 cm^{-1} are the most distinguishing features. Sharp asymmetric peaks at 719 to 725 and 3,516 cm^{-1} with a broad peak at 1,389 can be used to determine the presence of β-FeOOH. The 309 cm^{-1} and 388 cm^{-1} peaks are also useful in determining the presence of β-FeOOH, however, these peaks are somewhat broad and are similar to the Raman peaks for other oxides and oxyhydroxides. The Raman spectra for Fe_3O_4 has only three peaks and of these only the 667 peak is consistently distinguishable. It should be noted that the Raman spectra for Fe_3O_4 is much less intense than the spectra of most of the other oxides and oxyhydroxides. The Raman spectra for γ-Fe_2O_3 has some minor peaks in the 260 cm^{-1} to 510 cm^{-1} range. The most intense peaks are broad peaks centered at 717 cm^{-1} and 1,412 cm^{-1}. Several other peaks are also present in the 2,580 cm^{-1} to 3,910 cm^{-1} range.

Raman spectra of iron sulfides used as standards for identifying the corrosion products formed on the test specimens are shown in Figures A-1. The

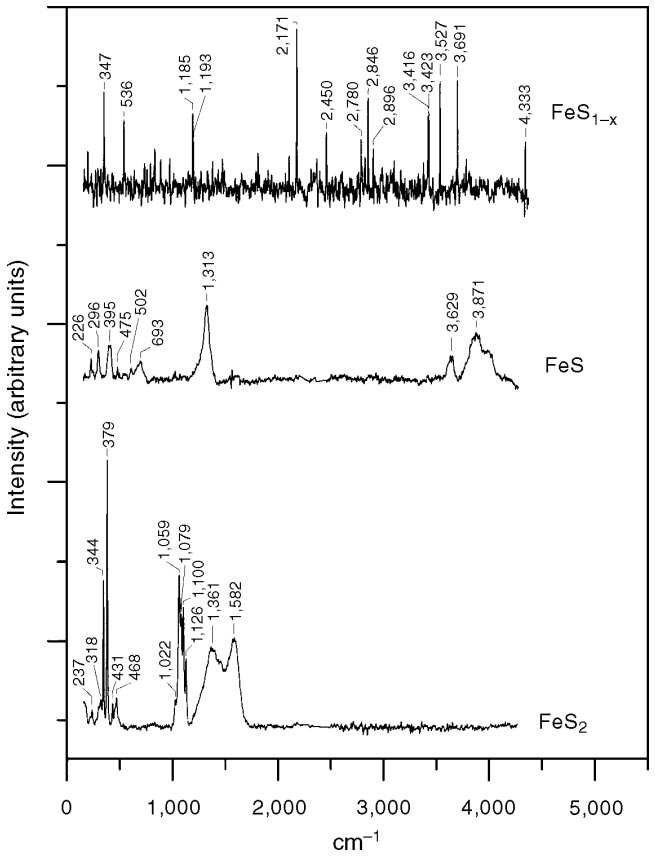

FIGURE A-1. *Raman spectra of iron sulfides. Spectra obtained with a 532-nm system using a laser power of 2 mW. Intensity scales are arbitrary.*

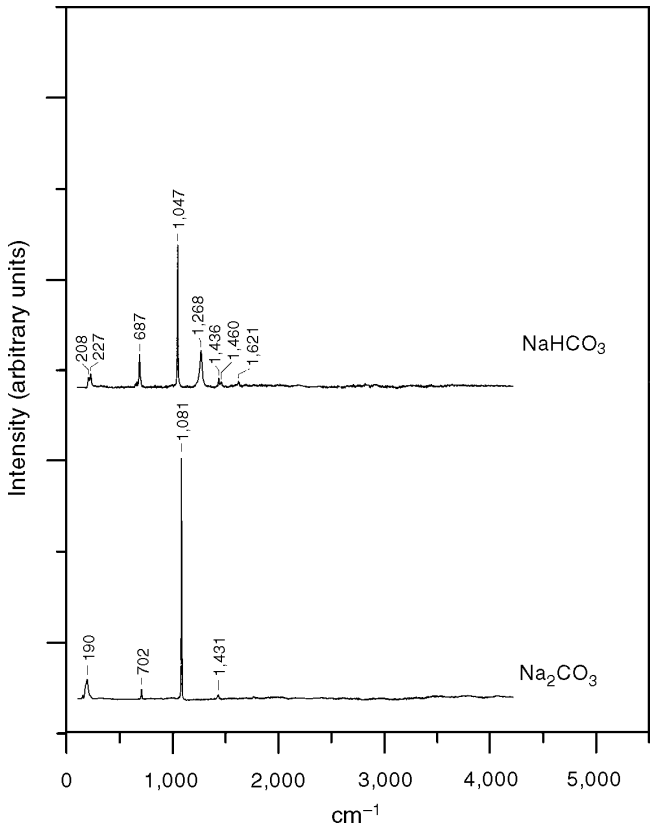

FIGURE A-2. *Raman spectra of $NaHCO_3$ and Na_2CO_2 spectra obtained with a 532-nm system using a laser power of 2 mW. Intensity scales are arbitrary. A strong peak located around 1,080 cm^{-1} is common for most carbonate minerals.*

spectra for Fe_2S, which is not expected to form under the conditions used in this study, has very well defined peaks at 344 cm^{-1} and 379 cm^{-1}. A group of 5 peaks is located in the range of 1,022 cm^{-1} to 1,126 cm^{-1}. The spectra for FeS (troilite or pyrrhotite), on the other hand, does not have such strong sharp peaks and is quite similar to the spectra obtained for γ-FeOOH. The spectrum for mackinawite has many sharp peaks. The strongest peaks are located at 347, 2,171, 2,846, 3,527, and 3,691 cm^{-1}. The spectrum of mackinawite shown in Figure A-1 is also noticeably noisier than the other iron sulfide spectra. The reference spectrum for Fe_3S_4 was not obtained in this study.

The spectra shown in Figure A-2 are of sodium carbonate (Na_2CO_3) and sodium bicarbonate ($NaHCO_3$). One of the test solutions used in this investigation contained $NaHCO_3$. The spectrum for Na_2CO_3 is quite similar to most other spectra for carbonate minerals including $FeCO_3$ and $CaCO_3$. All of these carbonate minerals have a strong sharp peak at 1,080 cm^{-1} to 1,090 cm^{-1}. The spectrum for $CaCO_3$ has an additional peak at 280 cm^{-1} while $FeCO_3$ has additional peaks at 290 cm^{-1} and 508 cm^{-1}.